https://doi.org/10.5194/egusphere-2023-2640
Preprint. Discussion started: 18 December 2023

Diagnosing Ozone-NO_x-VOCs-Aerosols Sensitivity to Uncover Urban-nonurban Discrepancies in Shandong, China using Transformer-based High-resolution Air Pollution Estimations

Chenliang Tao[1], Yanbo Peng[1,2,], Qingzhu Zhang[1,*], Yuqiang Zhang[1], Bing Gong[3], Qiao Wang[1], Wenxing Wang[1]*

[1]Big Data Research Center for Ecology and Environment, Environmental Research Institute, Shandong University, Qingdao 266237, P.R. China

[2]Shandong Academy for Environmental Planning, Jinan 250101, P. R. China

[3]Jülich Supercomputing Centre, Forschungszentrum Jülich, 52425 Jülich, Germany

Keywords:

Air pollution, Deep learning, Transformer, Satellite, Urban-rural difference, Ozone Regime

*Corresponding authors. E-mail: zqz@sdu.edu.cn, pengyanbo@mail.sdu.edu.cn

https://doi.org/10.5194/egusphere-2023-2640
Preprint. Discussion started: 18 December 2023

Abstract

Narrowing surface ozone disparities between urban and nonurban areas escalate health risks in densely populated urban zones. A comprehensive understanding of the impact of ozone photochemistry processes on this transition remains constrained by our knowledge of aerosol effects and the spatial availability of surface monitoring. Here we developed a novel deep learning framework, which could perceive spatiotemporal dynamics from adjacent grids by multidimensional self-attention operation, integrating multi-sources data to estimate daily 500 m surface ozone, nitrogen dioxide (NO_2) and fine particulate matter ($PM_{2.5}$) concentrations. Subsequently, three distinct ozone formation regimes linked with its precursors, aerosols, and meteorology were delineated through an interpretable machine learning method. The evaluations of the framework exhibited average out-of-sample cross-validation coefficient of determination of 0.96, 0.92 and 0.95 for ozone, NO_2 and $PM_{2.5}$, respectively. In 2020, urban ozone levels in Shandong surpassed those in nonurban due to a more pronounced decrease in ozone in the latter where $PM_{2.5}$ is the dominant anthropogenic driver. The ozone sensitivity to volatile organic compounds (VOCs), the dominant regime in urban areas, was observed to shift towards a NO_x-limited when extended to rural areas. A third 'aerosol-inhibited' regime was identified in the Jiaodong Peninsula, where the uptake of hydroperoxyl radicals onto aerosols suppressed ozone production under low NO_x levels during summertime. The reduction of $PM_{2.5}$ would increase the sensitivity of ozone to VOCs, necessitating more stringent VOC emission abatement for urban ozone mitigation. Our case study demonstrates the critical need for advanced modeling approaches providing finer spatially resolved estimations.

https://doi.org/10.5194/egusphere-2023-2640
Preprint. Discussion started: 18 December 2023

1. INTRODUCTION

Surface ozone (O_3), fine particulate matter ($PM_{2.5}$) and nitrogen dioxide (NO_2) are among the most important trace gases in the atmosphere that significantly impact the ecological environment and public health (Han and Naeher, 2006; Yue et al., 2017). During the Action Plan on the Prevention and Control of Air Pollution (denoted as the Clean Air Action, 2013-2017) (Action Plan on Air Pollution Prevention and Control (in Chinese), 2023), $PM_{2.5}$ and nitrogen oxide (NO_x = nitric oxide (NO) + NO_2) emissions across China decreased by 33% and 21% respectively (Zheng et al., 2018), while surface O_3 exhibited an increasing trend (Lu et al., 2018). The increase in O_3 could be partially attributed to the "aerosol-inhibited" effect, where the reduction in $PM_{2.5}$ results in a diminished reactive uptake of hydroperoxyl radicals (HO_2) onto aerosol (Ivatt et al., 2022; Li et al., 2019). The societal benefits of reducing premature deaths and economic losses from $PM_{2.5}$ reductions have been diminished by the rising O_3 (Liu et al., 2022). Thus, achieving the joint attainment objectives for $PM_{2.5}$ and O_3 has been put on the top priority of China's long-term air pollution control policies.

The complexity of the O_3 formation is partly reflected by the nonlinear response to changes in precursors (i.e. volatile organic compounds (VOCs) and NO_x), as well as the presence of heterogeneous reactions in aerosols. Understanding these dynamics is crucial to investigate the narrowing differences in O_3 concentrations between urban and nonurban areas, which have traditionally shown higher levels in rural (Han et al., 2023). The formaldehyde-to-NO_2 ratio (HCHO/NO_2 or FNR) serves as a theoretical gauge of

https://doi.org/10.5194/egusphere-2023-2640
Preprint. Discussion started: 18 December 2023

the relative abundance of total organic reactivity to hydroxyl radicals (OH) and NO_x (Wei et al., 2022c; Sillman, 1995), and as such, it can function as a useful indicator of O_3 sensitivity. Previous studies have utilized the $HCHO/NO_2$ from satellite remote sensing to infer O_3 production regimes for guiding O_3 control policies (Jin et al., 2023; Li et al., 2021a; Jin et al., 2020). However, the changes of $HCHO/NO_2$ threshold in O_3 regimes classification modulated by meteorology and localized atmospheric chemistry in space and time, and uncertainties relating column to surface, precluding robust applications over larger spatial scales (Lee et al., 2023; Jin et al., 2017; Souri et al., 2023). While the observation-based model method alleviates some of these limitations, constraints remain including computational demands and priori chemical mechanisms (Song et al., 2022b; Chu et al., 2023). The advent of interpretable machine learning models affords new opportunities to unravel intricate dependencies governing O_3 formation purely from actual observational data. However, sparse ground-based monitoring stations, especially in rural areas, pose great challenges to the spatially full coverage of studies. Thus, the high-spatiotemporal-resolutions estimations of surface air pollutants are urgently needed to improve our understanding of how these pollutants are changing and interacting.

Recent studies have utilized spatially resolved remote sensing data to estimate the continuous distribution of air pollutants in space by diverse machine learning (ML) models (Lyapustin and Wang, 2022; Lamsal et al., 2022; Huang et al., 2021; Li and Wu, 2021; Ren et al., 2022b), such as random forest (RF), full residual deep learning,

https://doi.org/10.5194/egusphere-2023-2640
Preprint. Discussion started: 18 December 2023

and Bayesian ensemble model. These attempts have demonstrated the tremendous potential of machine learning as an alternative to atmospheric chemical models (Jung et al., 2022). Nevertheless, there are still several aspects that have not been fully considered. For instance, coarse-resolution maps limit the ability to characterize the fine-scale variation of air pollution within urban areas, which has significant implications for environmental justice disparities of disadvantaged communities (Jerrett et al., 2005; Ren et al., 2022b; Dias and Tchepel, 2018). Additionally, existing machine learning models may not fully account for the complex atmospheric chemistry and physics processes that influence pollutant concentrations due to the single-pixel-based processing mode (Huang et al., 2021; Requia et al., 2020; Thongthammachart et al., 2022; Li et al., 2022b; Geng et al., 2021). Although several efforts have been made by using the neural network with convolutional layers (Di et al., 2016), and explicitly incorporating spatiotemporally weighted information to machine learning models (Wei et al., 2022b), the global spatio-temporal self-correlation of multi-dimensional features in the input array remained unaddressed. Meanwhile, the convolutional operations extract features from all neighboring grids of the target, ignoring the fact that the environmental knowledge of the target grid itself is the most significant, with the adjacent features being secondary.

Here, we developed a new spatiotemporal Transformer framework built exclusively on self-attention over space, time, and variables, termed Air Transformer (AiT), to reconstruct high spatiotemporal resolutions (daily, 500 m) estimations of

https://doi.org/10.5194/egusphere-2023-2640
Preprint. Discussion started: 18 December 2023

$PM_{2.5}$, O_3, and NO_2 from TROPOMI. In this framework, we paid special attention to air mass transport and dispersion affected by the spatial-temporal correlations, incorporated the downscaling mechanism from the model perspective, and considered the interactions between multiple pollutants from massive ground-level monitoring, satellite observations, meteorological conditions, dynamic industrial emissions, and other ancillary data. The explainable method (Shapley Additive exPlanations, SHAP) (Lundberg and Lee, 2017) was leveraged to provide insights into the impact of each environmental factor on air quality. The fidelity of the dataset was evaluated by comparing the spatial-temporal variations of RF (Breiman, 2001) estimations with the same variables and also the ChinaHighAirPollutants (CHAP) dataset (Wei et al., 2022b, 2020, 2022a). The spatial characteristics of air pollution from various emission sources and the urban-nonurban disparities across different cities are further examined to elucidate the potential values of high-resolution data. Surface O_3 formation regimes in Shandong provinces were inferred by the classic XGBoost model (Chen and Guestrin, 2016) coupled with SHAP, which identifies the impact of meteorology, $PM_{2.5}$, NO_2 and HCHO on O_3, in which HCHO was derived using the conversion factors algorithm based on the Tropospheric Ozone Monitoring Instrument (TROPOMI) and reanalysis of atmospheric composition. The new deep learning framework is expected to enable new applications like those of fine-scale air quality simulation, health exposure assessment, and O_3 formation regimes studies.

https://doi.org/10.5194/egusphere-2023-2640
Preprint. Discussion started: 18 December 2023

2. MATERIALS AND METHODS

2.1 Predictor Variables

The study domain covered the Shandong provinces of China with a high mortality burden of air pollution (Liu et al., 2017). The surface $PM_{2.5}$, O_3, and NO_2 concentration measurements were collected from the regulatory air quality stations of the China National Environmental Monitoring Center (CNEMC, with a total of 179 locations) and also the Shandong Provincial Eco-environmental Monitoring Center (SDEM, with a total of 166 locations) (Figure S1). The SDEM stations were included to fill the spatial gap in the county and rural areas where CNEMC stations were lacking. The study area was divided into 1.22 million grid cells with a spatial resolution of 500 m. We utilized a range of predictor data including tropospheric NO_2 vertical column densities (VCDs) and O_3 total VCDs measured by TROPOMI (Lamsal et al., 2022, 2020), aerosol optical depth (AOD) data and atmospheric properties obtained from Moderate Resolution Imaging Spectroradiometer (MODIS) Multi-Angle Implementation of Atmospheric Correction products (Lyapustin and Wang, 2022), AOD estimates from Modern-Era Retrospective Analysis for Research and Applications as the supplement of MODIS (2015), meteorological reanalysis data obtained from ERA5 (Hersbach et al., 2023, p.5), daily dynamic industrial emissions, moonlight-adjusted nighttime lights product (Román et al., 2018), vegetation index (Didan, 2021), population density (WorldPop, 2018), road density, land use data (Jun et al., 2014), and the shuttle radar topography mission digital elevation model. The detailed information for all the predictive variables

https://doi.org/10.5194/egusphere-2023-2640
Preprint. Discussion started: 18 December 2023

is listed in Table S1 and discussed in Text S1-2. Taking the space-variant and seasonal patterns into consideration, several spatiotemporal indicators such as geographical coordinates, Euclidean spherical coordinates, year, Julian date, and helix-shape trigonometric sequences were also included as predictor variables (Text S3) (Sun et al., 2022). Geographic Information Systems techniques including reprojection and resampling were used to consolidate all the data obtained for consistent projection and spatial scale. Finally, the Light Gradient Boosting Machine was used to fill satellite data gaps (Text S4) (Ke et al., 2017).

2.2 Air Transformer

AiT is an individual Transformer model that adopts encoder-decoder architecture with multidimensional self-attention computation to dynamically capture the spatiotemporal autocorrelation of atmospheric pollution changes from the sequences of pixels and variables for more reliable spatial maps of estimation. Compared with the existing image and video recognition Transformers, such as ViT (Dosovitskiy et al., 2021), Timesformer (Bertasius et al., 2021) and Uniformer (Li et al., 2021b), AiT is innovative in incorporating self-attention across channels after the self-attention based on pixels and taking advantage of the decoder. The former can capture the correlations between predictor variables. The decoder was employed to enable interaction between the primary target grid and neighboring grids. Predictor variables with 8-timesteps within 1000 m of the target grid cell were fed into the model to learn spatiotemporally disparities among atmospheric pollutants for predicting O_3, NO_2 and $PM_{2.5}$ within the

https://doi.org/10.5194/egusphere-2023-2640
Preprint. Discussion started: 18 December 2023

target grid point.

The overall architecture of the proposed AiT model and the dimension of input data are illustrated in **Figure 1**. The encoder maps an input sequence with neighborhood spatiotemporal data to a sequence with high-dimensional spatial-temporal characteristics, and the decoder generates an estimation by computing self-attention representations between the target grid and outputs of the encoder. The encoder of AiT takes as input a clip $X \in R^{V\times T\times H\times W}$ consisting of T multi-variables frames of size $H \times W$ sampled from the original dataset, where V is the number of variables and the target grid cell is located in $(\left\lceil \frac{H}{2} \right\rceil, \left\lceil \frac{W}{2} \right\rceil)$. The decoder takes as input a clip $X \in R^{V\times 1\times 1\times 1}$ consisting of V variables from the target grid. Several Transformer blocks with modified self-attention computation (AiT blocks) are applied to the encoder. The AiT encoder block is similar to the standard vision transformer block but specifically designed for atmosphere estimation (Dosovitskiy et al., 2021). It is a stack of two self-attention schemes including global spatiotemporal self-attention on the pixels and channel self-attention on variable predictors. The former contains $N = HW$ effective input sequence length for the self-attention to extract spatiotemporal information. The latter computes self-attention based on V effective input sequence length to capture hidden variables information. The decoder part is symmetric to the encoder part, while it only has a block with the spatiotemporal self-attention mechanism. We compute the matrix of self-attention outputs as:

$$Attention(Q,K,V) = \text{softmax}\left(\frac{QK^T}{\sqrt{d_k}} + \text{B}\right)\text{V} \quad (1)$$

https://doi.org/10.5194/egusphere-2023-2640
Preprint. Discussion started: 18 December 2023

where Q, K, and V are the queries, keys, and values are the inputs of the particular attention, respectively. d_k is the feature dimensionality of the K, and B is the geographic positional bias term. Another difference is that the attention function of the decoder is computed on Q from the estimated grid data, and $(K,\ V)$ from the outputs of encoder blocks under the same stage, resulting in the outputs of the last decoder block sized 1×128. The description of the data transformation and design details in the process of training can be found in Text S5. The multi-task learning strategy was also applied for learning representation across multiple pollutant estimation tasks (Text S6).

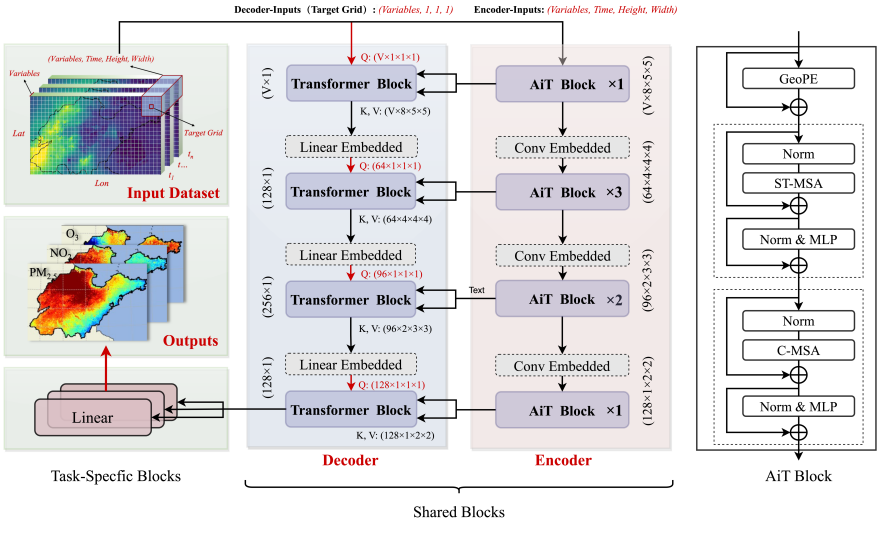

Figure 1. Schematic diagram of the AiT model. The white box of multi-dimension inputs presents each pixel of raster data. The AiT Block is a Transformer block based on self-attention across space, time and variables. The GeoPE, Norm, MLP, ST-MSA and C-MSA indicate respectively positional embedding, layer normalization, multi-layer perceptron, spatial-temporal multi-head self-attention and multi-channels (multi-variables) multi-head self-attention.

https://doi.org/10.5194/egusphere-2023-2640
Preprint. Discussion started: 18 December 2023

2.3 Diagnosing O_3 Formation Sensitivity

Interpretability can provide insight into how a model may be improved, bolster understanding of the process being modeled, and engender appropriate confidence from researchers. SHAP is a coalitional game theoretic approach based on Shapley values (Shapley, 1988) and then assigns each variable an importance value for a particular estimation. Deep SHAP, a high-speed approximation algorithm that builds on the connection between Shapely values and DeepLIFT (Shrikumar et al., 2019), is employed to compute the feature importance of AiT from all data with monitoring labels for interpreting the prediction. The sensitivity of the O_3 formation regime was deduced using a combination of the XGBoost model and SHAP interpretability method using the GPUTreeShap algorithm (Mitchell et al., 2020), which simulated the response of surface O_3 to meteorological conditions, HCHO, NO_2 and $PM_{2.5}$, by utilizing the continuous estimations from ERA5, AiT and TROPOMI between 2019 and 2020. The incorporation of meteorology in the model ameliorated the inadequacies in the conventional method (HCHO-NO_2 ratio) where its thresholds for identifying O_3 regimes vary temporally and spatially. The positive or negative contributions of three atmospheric pollutants were used to identify their promoting or inhibitory effect on O_3 variability. Given the unbiased property of SHAP values regarding directionality, the normalized relative magnitudes of SHAP values were calculated for HCHO (a proxy for VOCs), NO_2 (a proxy for NO_x) and $PM_{2.5}$ (a proxy for aerosols). This allowed differentiation of the O_3 formation regimes based on the locally maximal proportions

https://doi.org/10.5194/egusphere-2023-2640
Preprint. Discussion started: 18 December 2023

of the SHAP values for each species. The ground-level monthly HCHO concentrations were derived using a combination of column-to-surface conversion factor (CF) simulated from the ECMWF Atmospheric Composition Reanalysis 4 and the tropospheric HCHO VCDs obtained from the TROPOMI (Cooper et al., 2022; Su et al., 2022; Inness et al., 2019). A detailed description of the CF method as used here is discussed in Text S7. To ensure consistency in resolution between TROPOMI and AiT, we employed the oversampling method to downscale the TROPOMI VCDs to the resolution of AiT estimation, which has been proven to be effective in achieving finer resolution (Su et al., 2022; Cooper et al., 2022; van Donkelaar et al., 2015).

3. RESULTS AND DISCUSSION

3.1 Performance Evaluation for the AiT

3.1.1 Cross-validation Metrics

We evaluated the AiT performance based on the 10-fold cross-validation (CV) approach (Text S8), with correlation coefficient (R^2) measuring the extent to which model simulations explain variability in atmospheric pollutants, and root mean square errors (RMSE) and mean absolute errors (MAE) evaluating the bias/error of the estimates. As shown in **Figure 2**, out-of-sample CV daily ground-level O_3, NO_2 and $PM_{2.5}$ estimations are highly consistent with ground observations (R^2 = 0.96, 0.92, 0.95), indicating low uncertainties, with RMSE of 10.1, 4.7, and 8.5 μg/m^3 and MAE of 7.2, 3.5, and 5.3 μg/m^3 during the 2018-2021 period. The linear regression comparing the O_3 predictions versus observations yields a slope of 0.98 and an interception of 2.39,

https://doi.org/10.5194/egusphere-2023-2640
Preprint. Discussion started: 18 December 2023

249 which demonstrates that there is no systematic bias in the estimations. Meanwhile, as
250 shown in Figure S2, our AiT model works well in the individual-site scale with high
251 CV-RMSE for O_3, NO_2, and $PM_{2.5}$ (10.5 ± 8.6, 4.7 ± 1.1, and 8.3 ± 2.8 μg/m^3). In
252 general, AiT model is robust for multi-pollutant simultaneous estimations.

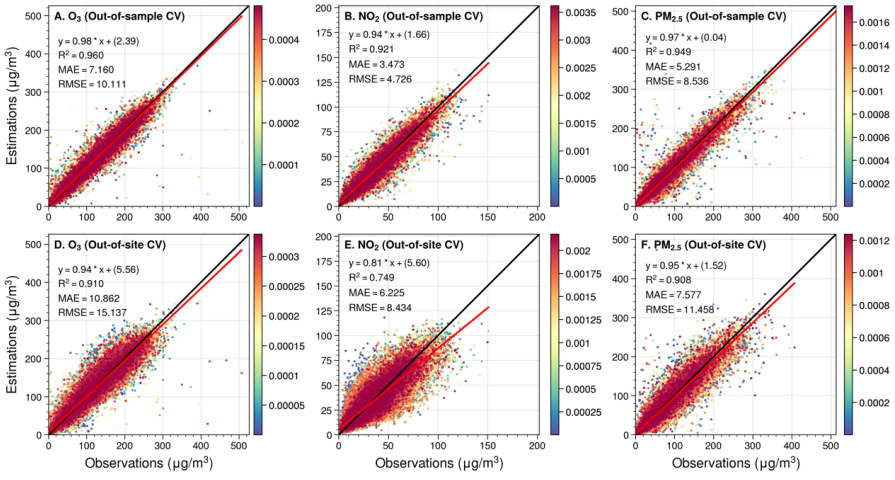

253

254 **Figure 2.** Out-of-sample cross-validation (A-C) and out-of-site cross-validation (D-F)
255 of daily ground-level O_3, NO_2 and $PM_{2.5}$ concentration in the validation set.

256 The spatial generalization ability of AiT is then examined by the out-of-site CV
257 evaluation method (**Figure 2**). The daily spatial variations of O_3, NO_2, and $PM_{2.5}$ at
258 locations where there are no ground measurements can be well estimated by our model
259 (i.e., CV-R^2 = 0.91, 0.75, 0.91), which is a core contribution of such studies. We also
260 probe the model performance for each site separately based on spatial CV estimations
261 (Figure S3). This general model yields RMSE of 15.2 ± 8.8, 8.1 ± 2.7, and 11.1 ± 2.8
262 μg/m^3, respectively. Furthermore, we trained AiT model using data exclusively from
263 CNEMC and assessed its generalizability by validating it with data from SDEM. The

https://doi.org/10.5194/egusphere-2023-2640
Preprint. Discussion started: 18 December 2023

model demonstrates strong performance with high R^2 values in the validation dataset of CNEMC (Figure S4), and when evaluated with SDEM data, it exhibits only a slight degradation in predictive accuracy (R^2 for O_3, NO_2, and $PM_{2.5}$: 0.95, 0.89, 0.85). Meanwhile, our framework utilizes multi-task learning to enhance computational efficiency through a single iteration and leverages the interactions among multiple pollutants to optimize the performance of individual pollutant levels (Table S2). In summary, AiT provides relatively stable estimations in areas without available ground-level monitoring values and reliably extends ground monitoring from the site scale to the full-coverage spatial scale with high spatial resolution.

3.1.2 Compared with Other ML Models

Since the ground-level air quality measurements across the target regions are extremely limited at 500 m spatial resolution, representing only roughly two-thousandths of the total grid cells, we seek implicit approaches to validate our estimated near surface pollutants concentrations. We compared the model performance with previous studies that applied different ML methods to estimate these three air pollutants individually and found out that our cross-validation results are comparable or even better than those (Table S3). We also created a new dataset in our study by applying the classic RF algorithm which is the most common ML model for estimating atmospheric pollution in recent years (Wei et al., 2022a; Requia et al., 2020; Xiao et al., 2018; Geng et al., 2021; Lu et al., 2021) with the same variables as AiT. The statistics comparisons between AiT and RF are also shown in Table S3. We then compared the spatial

https://doi.org/10.5194/egusphere-2023-2640
Preprint. Discussion started: 18 December 2023

distribution of our results with estimations from CHAP.

Figure 3 shows the spatial maps of near-surface air pollutants with partially zoomed satellite images for monitoring sites, AiT, RF and CHAP in 2019 (see Figure S6 for 2020). We found that the estimated NO_2 and $PM_{2.5}$ from the AiT share a similar spatial distribution as those estimated by RF and CHAP. However, enlarged city-level urban regions in **Figure 3** reveal that AiT estimates fine structures and intra-urban disparities in near-surface multi-pollutant concentrations which cannot be captured by either RF or CHAP products. In general, while RF and CHAP can only see the hotspots of air pollutants at a regional scale, the spatial distribution of air pollutants estimated by the AiT shows much more detailed differences with high spatial and temporal variability across the city scale. The difference of near-surface annual averaged pollutants between 2019 and 2020 for measured and multi-estimated data were presented in Figure S7. The reductions or increments of O_3, NO_2 and $PM_{2.5}$ in distinct locations can be simulated by our model, which is relatively consistent with the change of measurements. The zoomed maps of Figure S7 show the difference in three pollutant concentrations at the city scale of the capital of Shandong Province, Jinan. It can be found that the change in pollutant levels in 2020 compared to 2019 exhibits substantial regional variations and intra-urban heterogeneity, with some areas experiencing an increase while others a decrease. Compared to estimations of RF and CHAP, our results successfully capture the complex distribution of air pollution in reality and reveal that the decline of $PM_{2.5}$ is primarily concentrated in suburban areas, while an increase is

https://doi.org/10.5194/egusphere-2023-2640
Preprint. Discussion started: 18 December 2023

306 pronounced in some regions of urban during 2020. Notably, this spatial trend may be
307 consistent with the underlying emission patterns and meteorological conditions.

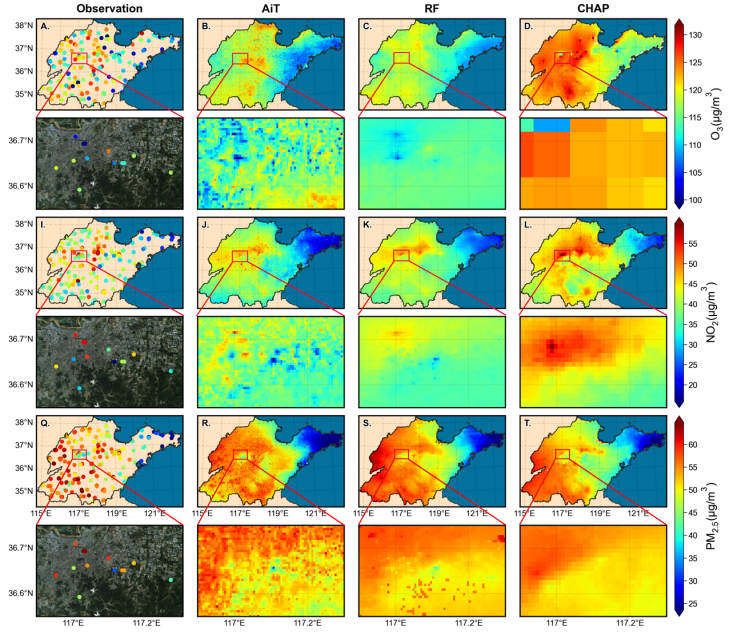

308

309 **Figure 3.** Spatial distribution of the annual mean (A-D) O_3, (I-L) NO_2 and (Q-T) $PM_{2.5}$
310 concentrations from observations, Air Transformer (AiT), Random Forest (RF) and
311 ChinaHighAirPollutants (CHAP), respectively, in 2019. The region enclosed by the red
312 rectangular box in (A-T) corresponds to the zoomed-in maps of satellite (© Tianditu:
313 www.tianditu.gov.cn) and pollutant concentrations at a city scale for the capital city of
314 Shandong Province, Jinan

315 **3.1.3 Typical Event Study**

316 The typical example of the spatial distribution of multi-pollutant observations and
317 estimations of AiT is compared for validating the predictive capability of the model at
318 a particular pollution episode, i.e., 13-16 March 2021. During this period, an early
319 season dust storm, which was called the largest and strongest such storm in a decade,

https://doi.org/10.5194/egusphere-2023-2640
Preprint. Discussion started: 18 December 2023

hits northern China (Myers, 2021). As shown in Figure 4, our model can capture the spatial distribution of surface O_3, NO_2 and $PM_{2.5}$ in the time of severe atmospheric pollution. In addition, our estimations are highly concordance with measurements in terms of magnitudes and spatial variability over the entire research region. Combined wind fields to analyze $PM_{2.5}$ distribution on the day of the dust storm, it can be found that surface wind carries a massive amount of particulate matter from Beijing, which suffered a severe dust storm, to northern Shandong. The influence was gradually diminishing in southern Shandong due to the obstruction of Mount Tai. Spatial heterogeneity within intra-urban was further investigated to identify the hotspots of pollution sources. The satellite images in even-numbered rows of Figure 4 illustrate the spatial disparities of three pollutants around four typical emission sources: thermal power plants, industrial parks, overpasses and parks. As depicted, these anthropogenic emission sources contribute to higher pollution levels, while the mountain in the park mitigates primary pollution but increases O_3 concentrations. Industrial sources emit a large number of NO_x and $PM_{2.5}$, leading to increased pollution of these species compared with other urban microenvironments, which in turn promotes O_3 formation, particularly in downwind areas (Miller et al., 1978; Tang et al., 2020). Although the spatial gradients of pollutants on the street are not as apparent as in the dataset with 100 m resolution (Huang et al., 2021), the predicted spatial variation between various geographical scenes is in satisfactory agreement given the 500 m scale of the model. Urban areas affected by diverse dust pollution exhibit lower $PM_{2.5}$ concentrations

https://doi.org/10.5194/egusphere-2023-2640
Preprint. Discussion started: 18 December 2023

341 compared to rural due to the obstructive and filtering effects of artificial structures such
342 as buildings and urban greenery (Figure S8), which cannot be effectively captured
343 solely by ground-based observations. Notably, the elevated $PM_{2.5}$ inhibits the formation
344 of O_3 by diminishing solar radiation flux and absorbing the HO_2 radical on the aerosol
345 surface, even in conditions characterized by similar NO_2 levels. As the mapping, AiT
346 accurately grasps the spatial characteristic of air pollutants and delivers a coherent
347 spatial-temporal distribution that is consistent with the prior knowledge of atmospheric
348 transport.

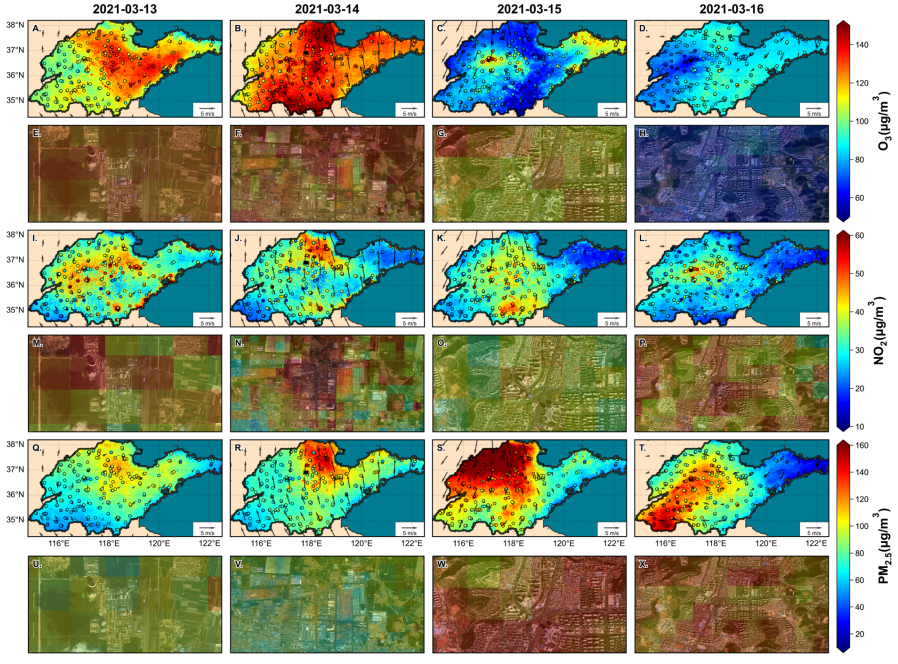

349

350 **Figure 4.** The spatial distribution of ground-level O_3 (A-D), NO_2 (I-L), and $PM_{2.5}$ (Q-
351 T) concentrations from AiT and monitoring stations during 13-16 March 2021 in
352 Shandong, China. The black arrows are the 10 m wind speed and wind direction. The
353 even-numbered rows correspond to the concentration distribution maps of typical
354 emission sources for the respective pollutants, accompanied by satellite images (©
355 Tianditu: www.tianditu.gov.cn). The upper right area of E, I, and Q is a thermal power

https://doi.org/10.5194/egusphere-2023-2640
Preprint. Discussion started: 18 December 2023

plant in Weifang City (119°250′E-119°280′E, 36°658′N-36°673′N). The center area of F, N, and V is an industrial park in Zibo city (117°725′E-117°845′E, 36°880′N-36°940′N). The center and upper right area of G, O, and W is an overpass and Wanling mountain in Jinan city (116°977′E-117°009′E, 36°590′N-36°606′N). The center area of H, P, and X is another overpass in Jinan city (116°970′E-117°030′E, 36°580′N-36°610′N).

3.2 Urban-nonurban Difference

The advantage of full-coverage pollutant estimates is the ability to assess the difference between urban and non-urban areas on a finer scale. Table S4 shows the concentrations of O_3, NO_2, $PM_{2.5}$ and HCHO over the urban and nonurban regions, delineated from an annual urban extents dataset (Zhao et al., 2022). From 2019 to 2020, surface air pollutant levels declined significantly in Shandong. The averaged concentration discrepancies of these pollutants between urban and non-urban over February to March (lockdown during COVID-19) and June to October (summertime) as shown in **Figure 5**. Surface concentrations in NO_2 and HCHO are higher in urban than nonurban areas, and the differences narrowed from February to October, while $PM_{2.5}$ is opposite at both. The ground-level O_3 levels exhibited unexpected urban-nonurban disparity variations, from the lockdown period through the summer, as well as from 2019 to 2020. In comparison to nonurban areas, the urban, which previously had lower O_3 levels, began to experience higher concentrations, attributed to a more rapid decline of ozone in nonurban regions. **Figure 6** revealed that urban-nonurban differences in O_3 and $PM_{2.5}$ varied across various cities during the lockdown period in 2019, while the higher NO_2 pollution in urban remained consistent. In summer, only a handful of urban areas exhibit lower levels of ozone concentration, where NO_2 and

https://doi.org/10.5194/egusphere-2023-2640
Preprint. Discussion started: 18 December 2023

$PM_{2.5}$ levels surpass those in nonurban regions, attributable to a more pronounced titration effect of NO and a slower rate of photochemistry reactions (Figure S9) (Sicard et al., 2016, 2020; Zhang et al., 2004). Comparative urban-nonurban differences from 2019 to 2020 indicate an accelerated reduction of ozone and HCHO in non-urban areas, while NO_2 and $PM_{2.5}$ levels in urban have seen a more significant decrease due to the decline in anthropogenic activities, particularly the suspension of emissions from pollution sources located in urban areas. Upon comparing the results of urban-nonurban disparities of our data with monitoring data and the CHAP dataset, we have identified potential overestimations or underestimations across various cities in monitoring data, likely resulting from the limited number of non-urban sites (**Figure 6**M, S10). The urban-nonurban difference calculated by the CHAP generally aligns with our findings (Figure S11). Nevertheless, it is worth noting that the coarse resolution of O_3 (10 km) has led to a significant overestimation. These results highlight the invaluable value of high-resolution and gapless data for studying urban-nonurban disparities.

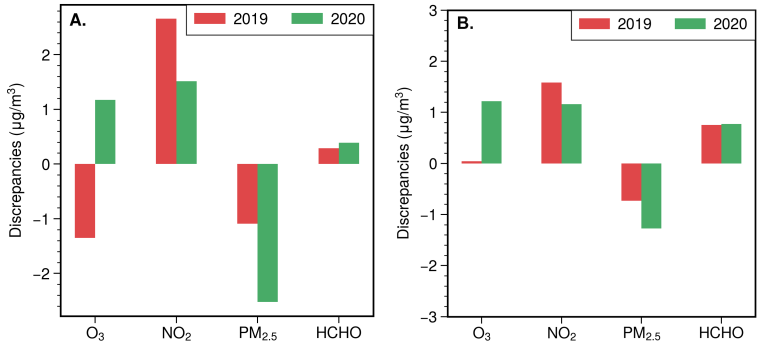

Figure 5. The discrepancies of O_3, NO_2 and $PM_{2.5}$ between urban and non-urban from 2019 to 2020 for the lockdown period (A) and summertime (B) averaged concentration.

https://doi.org/10.5194/egusphere-2023-2640
Preprint. Discussion started: 18 December 2023

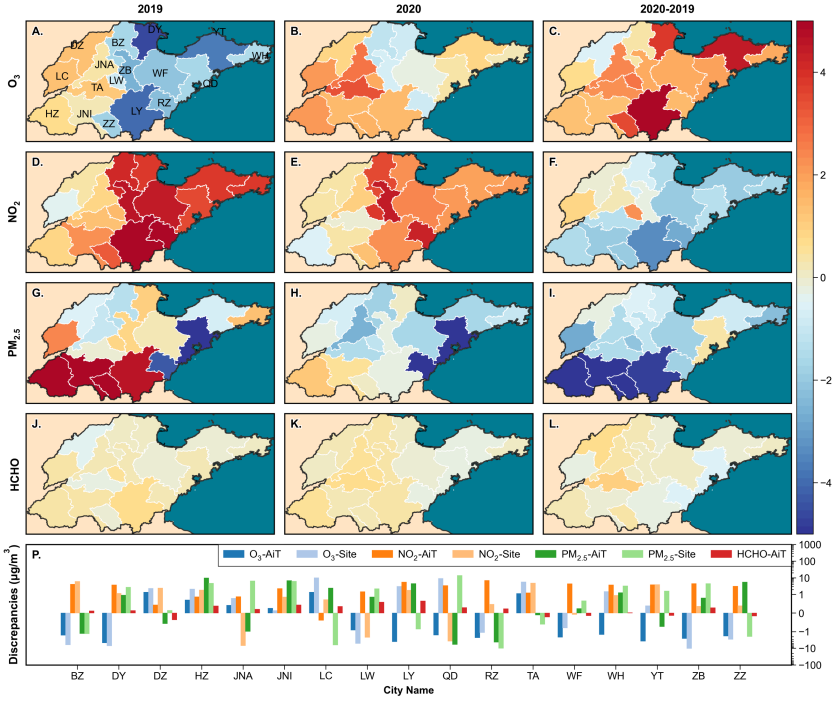

Figure 6. The urban-nonurban disparities of O_3, NO_2, $PM_{2.5}$ and HCHO calculated by AiT across cities with administrative divisions in Shandong, China during lockdown periods in 2019 (A, D, G) and 2020 (B, E, H), and the changes of differences between 2019 and 2020 (C, F, I). M is the comparison between the results of monitoring station data and AiT dataset in 2019. The red color represents a greater decline in air pollutants in nonurban areas, while the blue color indicates a more significant reduction in urban areas in the third column of the figure. (YT: Yantai, BZ: Binzhou, DY: Dongying, WH: Weihai, DZ: Dezhou, JNA: Jinan, QD: Qingdao, WF: Weifang, ZB: Zibo, LC: Liaocheng, LW: Laiwu, TA: Taian, LY: Linyi, RZ: Rizhao, JNI: Jining, HZ: Hezhe, ZZ: Zaozhuang)

3.3 Photochemical Regimes

3.3.1 Ozone-NO_x-VOCs-Aerosols Sensitivity

Figure S12 shows the seasonal maps of O_3, $PM_{2.5}$ and NO_2 estimations from AiT, satellite-derived surface HCHO. Based on these data, we first capture the well-established non-linearities in O_3-VOC-NO_x chemistry by a conceptual framework

https://doi.org/10.5194/egusphere-2023-2640
Preprint. Discussion started: 18 December 2023

similar to classic O_3 isopleths typically generated with models (Pusede et al., 2015; Ren et al., 2022a). **Figure 7**a depicts O_3 concentration as a function of HCHO and NO_2, which was derived solely from ground-level estimation. The result indicates that the O_3 regimes can be qualitatively identified based on the nonlinear interaction between surface O_3, HCHO and NO_2. In the regime characterized by high NO_2 and low HCHO, the elevated consumption of HO_x, predominantly driven by the OH + NO_2 termination reaction, results in the suppression of NO_x on O_3, indicating the prevalence of VOC-limited chemistry. Conversely, when HCHO levels are high and NO_2 levels are relatively low, O_3 increases with NO_2 and exhibits insensitivity to HCHO due to abundant peroxyl radicals (HO_2 + organic peroxy (RO_2) radical, RO_x) self-reactions, suggesting a NO_x-limited (VOC-saturated) chemistry. In the case of high HCHO and NO_2, the O_3 increases with both HCHO and NO_2, reaching a peak. While **Figure 7**a resembles this overall O_3-VOC-NO_x, the blurry transition between two different regimes and the role of $PM_{2.5}$ is uncertain which may be influenced by meteorological conditions, chemical and depositional loss of O_3, errors of estimations, and "aerosol-inhibited". Increased $PM_{2.5}$ levels could suppress O_3 formation even under high HCHO and NO_2 conditions (**Figure 7**b), which could be induced by enhanced reactive uptake of HO_2 onto aerosol particles and weaker photochemical reaction resulting from the scattering and absorption of solar radiation by anthropogenic aerosols. The relationship between $PM_{2.5}$ and O_3 in Shandong demonstrated the distinct stages of O_3 chemistry, as depicted in **Figure 7**c. When $PM_{2.5}$ was below the maximum turning point (MTP1, 35

https://doi.org/10.5194/egusphere-2023-2640
Preprint. Discussion started: 18 December 2023

μg/m^3), a linear and positive correlation between O_3 and $PM_{2.5}$ was observed due to the common dependence on their precursors in the initial stage (Zhang et al., 2022). As $PM_{2.5}$ increased beyond the MTP1, a sharp reduction in HCHO and O_3 was observed, accompanied by a decline in surface short-wave radiation, which reflect their formation as a photo-oxidation product of OVOCs and NO_x. When $PM_{2.5}$ exceeded the minimum transition point (MTP2, 45 μg/m^3), a phase was observed with stagnant radiation intensity and relatively higher NO_2 levels compared to HCHO. This regime is typically associated with a VOC-limited regime, where increased HCHO and decreased NO_2 concentration could promote O_3 production. However, our findings demonstrated an opposite impact of HCHO and NO_2 on O_3 when $PM_{2.5}$ beyond MTP2. **Figure 7**d shows the changes in the quantitative relationships between HCHO/NO_2 (FNR) and O_3 by artificially changing $PM_{2.5}$ and precursors levels for XGBoost, in which the peak of curves marks the transitional threshold of O_3 regimes from VOC to NO_x sensitive. It can be seen that attenuated $PM_{2.5}$ pollution could increase the sensitivity of O_3 to VOCs and decrease the sensitivity to NO_x, which causes the shift in O_3 regimes from NO_x-limited to VOC-limited. With the recent reduction in NO_x emission in China, the anticipated transition of O_3 production regime in urban areas towards more NO_x-limited has been impeded by the heightened VOC sensitivity resulting from decreased $PM_{2.5}$ levels. Our results are consistent with the findings of Li et al. on the O_x-NO_x relationship in response to changing $PM_{2.5}$ (Li et al., 2022a), and the findings of Dyson et al. on the impact of HO_2 aerosol uptake on O_3 production (Dyson et al., 2023). The SHAP

https://doi.org/10.5194/egusphere-2023-2640
Preprint. Discussion started: 18 December 2023

455 interaction values between $PM_{2.5}$ and the other two variables, HCHO and NO_2,
456 demonstrated that lower NO_2 and higher HCHO levels could diminish the formation of
457 O_3 under high $PM_{2.5}$ concentrations due to enhanced titration of O_3 by NO resulting
458 from weaker conversion from NO to NO_x through RO_x radical (**Figure 7**e, f). It further
459 illustrates that the scavenging of HO_2 on aerosols can cause the shift of O_3 regimes from
460 being VOC-limited to NO_x-limited and the threshold approach is restricted by aerosol
461 and meteorology for determining the constantly changing O_3 formation regimes over
462 time and space.

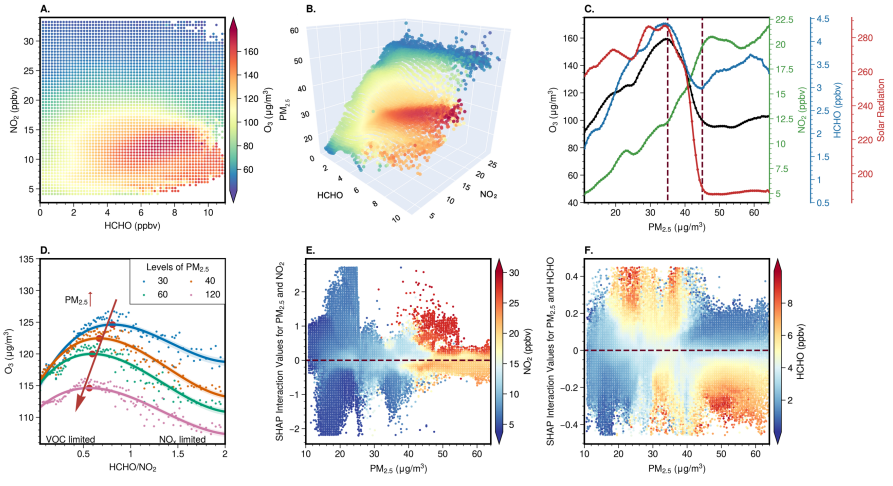

463
464 **Figure 7.** (A) O_3 concentrations as a function of surface HCHO and NO_2. (B) O_3
465 concentrations as a function of surface HCHO, NO_2 and $PM_{2.5}$. (C) Relationship
466 between O_3, and NO_2, HCHO and surface short-wave radiation flux. The paired O_3,
467 HCHO, NO_2 and solar radiation are divided into 100 bins based on $PM_{2.5}$ and then the
468 averaged concentrations (y-axis) are calculated for each $PM_{2.5}$ bin (x-axis). (D)
469 Changes in HCHO/NO_2-O_3 relationship in response to changing $PM_{2.5}$ by XGBoost
470 model. The solid lines are fitted with four-order polynomial curves, and the shading
471 indicates 95% confidence intervals. (E-F) The interaction SHAP values reveal an
472 interesting hidden relationship between pairwise variables ($PM_{2.5}$ and NO_2, HCHO) and
473 O_3.

https://doi.org/10.5194/egusphere-2023-2640
Preprint. Discussion started: 18 December 2023

Unraveling the intricate interplay of O_3 on meteorology, aerosol and precursors that govern O_3 formation over extensive spatial domains has long confounded robust interpretation. These multiscale processes were elucidated by using an interpretable ML model, which can quantify the positive or negative contributions of individual processes. Figure S13 elucidates that meteorological variations, chiefly surface short-wave radiations flux modulating photochemical reaction kinetics, primarily dictate the heterogeneous geographic distribution of O_3 at the regional scale, with lower levels over Jiaodong Peninsula. Meanwhile, local atmospheric chemical processes predominate the city-scale variability of O_3. HCHO facilitated O_3 formation in urban areas yet suppressed it in rural regions across areas with high ozone, where most NO_2 promoted O_3 production overall, indicating VOC-NO_x synergistic control on O_3 in cities and a NO_x-limited regime in rural areas during summertime. The contribution of NO_2 and $PM_{2.5}$ exhibits analogous seasonal variability, promoting O_3 formation under low pollution conditions while inhibiting O_3 when pollution levels are high (Figure S12, 14). The elevated NO_2 levels in autumn led to a negative contribution to O_3, whereas the facilitating effect of $PM_{2.5}$ was enhanced. This stems from the relatively moderate $PM_{2.5}$ concentrations slightly affecting photochemical reaction rates, while the increased NO_2 amplified the reactive uptake of NO_2 by $PM_{2.5}$, generating more OH radicals that promote O_3 formation (Lin et al., 2023; Tan et al., 2022). In winter, $PM_{2.5}$ pollution exceeding 75 $\mu g/m^3$ suppressed O_3 formation through scattering and absorbing solar radiation that activates atmospheric chemical processes, which

https://doi.org/10.5194/egusphere-2023-2640
Preprint. Discussion started: 18 December 2023

495 counteracted the promoting effect of high $PM_{2.5}$ through the conversion of NO_2 to
496 HONO.

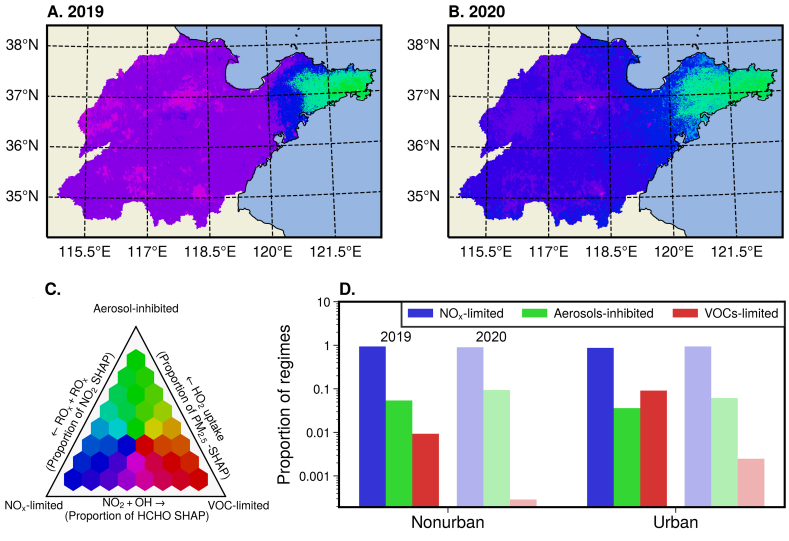

497

498 **Figure 8.** Comparison of geographical distribution for ozone formation regimes
499 between 2019 and 2020 in the summertime. All surface daily O_3, $PM_{2.5}$ and NO_2
500 estimations from Air Transformer (AiT) are averaged over each month from May to
501 October 2019-2020 for matching monthly HCHO derived from TROPOMI (500 * 500
502 m). (A, B) Geographical distribution of fractional contribution of chemical factors
503 representing O_3 formation regimes. (C) The ternary phase diagram depicts the
504 normalized fraction of SHAP values for O_3 attributed to HCHO, NO_2, and $PM_{2.5}$ at the
505 surface, representing VOC-limited (red), NO_x-limited (blue) and aerosol-inhibited
506 (green) regimes. (D) The proportion and changes of three regimes across urban and
507 nonurban areas in Shandong between 2019 and 2020.

508 **Figure 8** shows the ternary phase diagram and surface distribution of the relative
509 proportion of SHAP values on three pollutants for inferring the photochemical regimes
510 of O_3. More of urban regions in Shandong are pink, indicating a VOC-limited regime
511 where NO_2 + OH is the dominant termination step, which is consistent with the findings
512 of previous studies on major cities (Ren et al., 2022a). Moving along an urban-to-rural

https://doi.org/10.5194/egusphere-2023-2640
Preprint. Discussion started: 18 December 2023

gradient, reactions dominated by RO_x radical self-reactions continuously enhanced with the increasing NO_x SHAP values, resulting in the majority of rural Shandong being situated in NO_x-limited regimes. Furthermore, the overall ozone production regimes in Shandong exhibited a transition toward more NO_x-limited from 2019 to 2020, with regions dominated by NO_x-limited shifting toward aerosol-inhibited in the Jiaodong Peninsula. The aerosol-inhibited regime differs from either of the two classically applied tropospheric O_3 policy-control regimes. It is attributed to predominant heterogeneous HO_2 uptake by aqueous aerosols, despite comparatively low $PM_{2.5}$ levels during summertime. The marine environment engenders liquid aerosol particles with HO_2 uptake coefficients exceeding those of dry aerosols by orders of magnitude (Song et al., 2022a). Concurrently, lower ambient NO_x levels minimize the promotive effects of aerosols on ozone formation (Tan et al., 2022; Kohno et al., 2022). This result is consistent with the results of Dyson et al. (Dyson et al., 2023), which concluded that the contribution of HO_2 sinks onto aerosols on total HO_2 could increase for areas with low NO levels. The attenuated responsiveness of O_3 formation to VOCs induced by the uptake of HO_2 results in enhanced sensitivity of NO_x at the northwest boundary region of the Jiaodong Peninsula. Collectively, these processes delineate an aerosol-inhibited ozone production regime, reflecting the sensitivity of O_3 photochemistry to HO_2 sink in this coastal region.

3.3.2 Impact on Urban-nonurban Differences

We further explore the reversed O_3 differences by separating the individual

https://doi.org/10.5194/egusphere-2023-2640
Preprint. Discussion started: 18 December 2023

contribution of climate and anthropogenic changes using the interpretable machine learning model (**Figure 9**). The results demonstrate that atmospheric chemical processes and meteorological conditions commonly dominate the urban-nonurban discrepancies in O_3 levels. During the lockdown period, the diminished reduction in boundary layer height and radiation flux across urban areas, compared to nonurban areas in 2020, decelerated the expected decline of O_3 concentrations, leading to urban O_3 levels exceeding those of nonurban areas (Figure S15). Concurrently, a narrowing difference in urban and nonurban temperatures, despite an overall cooling from 2019 to 2020, favored O_3 formation in urban regions during the summertime. Additionally, PM2.5 emerged as the principal anthropogenic factor inverting the urban-nonurban O_3 disparity over the course of 2019 to 2020. Its contribution to ozone shifted from being lower in urban areas to exceeding that in nonurban areas, revealing that the decreased reactive uptake of HO_2 from aerosols induced by a more substantial reduction in $PM_{2.5}$ in urban areas made the larger contribution to O_3 production (Ivatt et al., 2022; Li et al., 2017). Meanwhile, the O_3 formation regimes also determine the response of O_3 to the changes in its precursors. The abatement of NO_x exhibited enhanced efficacy for O_3 mitigation in nonurban areas, which, in 2020, shifted predominantly toward a NO_x-limited regime, in contrast to urban regions that remained constrained by a more VOC-limited or oscillated between NO_x and VOCs regimes (**Figure 8**b). **Figure 8**d shows that urban regions, characterized by elevated NO_x emission, exhibited a higher proportion of VOC-limited, and the fraction of aerosol-inhibited areas increased from

https://doi.org/10.5194/egusphere-2023-2640
Preprint. Discussion started: 18 December 2023

555 2019 to 2020, resulting in the control benefits of urban O_3 pollution in 2020 are partially
556 offset by the nonlinear response of O_3 to a greater reduction in NO_2 and $PM_{2.5}$, and a
557 smaller decrease in HCHO relative to nonurban areas. Consequently, O_3 exhibits a
558 lower reduction in urban areas as a result of the aforementioned changes.

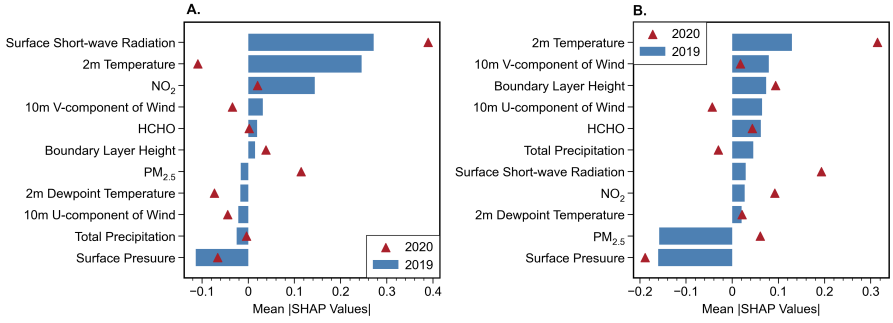

559

560 **Figure 9.** The changes of the mean absolute SHAP values disparities in urban-nonurban
561 from 2019 to 2020 across Shandong, China during the lockdown periods (A) and
562 summertime (B).

563 ## 4. CONCLUSIONS

564 Based on the evaluation of the non-linearity of O_3-NO_x-VOCs-aerosols chemistry
565 captured by interpretable ML model based on spatially resolved multi-pollutants
566 estimations, this study assesses three various chemical regimes by tracking NO_x, VOCs
567 and aerosols with surface NO_2, HCHO and $PM_{2.5}$. We conclude that with the effective
568 reduction of $PM_{2.5}$ pollution, the sensitivity of O_3 to VOCs will increase, necessitating
569 that government agencies further intensify the regulation of VOC emissions. In the
570 Jiaodong Peninsula of Shandong Province, coastal areas with relatively minor primary
571 pollutants are widely found to be under an aerosol suppression regime, illustrating that
572 ozone regime inference based on machine learning can serve as an alternative to

https://doi.org/10.5194/egusphere-2023-2640
Preprint. Discussion started: 18 December 2023

determining the aerosol suppression regime through the rate of radical termination in atmospheric chemical models. The O_3 regime in other areas of Shandong generally transited from the VOC-sensitive regime in urban to a more NO_x-sensitive regime in nonurban. We estimate that the substantial anthropogenic emission reduction of $PM_{2.5}$ and NO_2 is the main anthropogenic driver of the reversal of traditional urban-nonurban discrepancy in O_3 levels. This shift underlines the intricate balance between emission reduction and ozone formation mechanisms, suggesting that nuanced understanding and targeted interventions are necessary to manage and mitigate the health and environmental impacts of such disparities. To preclude exacerbated O_3 pollution resulting from the shift of many regions from NO_x-limited to VOC-limited regimes and the decline in heterogeneous HO_2 uptake induced by $PM_{2.5}$ reduction in urban areas, emission policies aimed at decreasing NO_x to reduce O_3 levels would only be effective with stringent VOC emission abatement when $PM_{2.5}$ is concurrently decreased.

Ozone formation is highly nonlinear, so accurate estimations are essential to infer its chemical regimes. The evaluation of model performance indicates that it can be readily extended to any other domain thanks to the unified architecture. Anyone can easily utilize the model to estimate ground-level pollutants that intelligently consider spatial-temporal neighborhood information based on their customized input data. Our model further improved the spatial resolution to sub-km using TROPOMI and MODIS retrievals via spatiotemporal autocorrelation downscaling of AiT. The “black box” AiT can be more physically interpretable by SHAP, enabling the evaluation of the

https://doi.org/10.5194/egusphere-2023-2640
Preprint. Discussion started: 18 December 2023

significance of each input variable (Figure S16). The season trends show the highest contribution, followed by emission proxies and meteorological conditions. The approach leads to these potentially surprising results that bring clarity to the growing space of methods.

Although our study endeavors to establish O_3 formation regimes involving NO_x, VOCs and aerosols, and the method identifies an aerosol inhibited from a statistical perspective, it is subject to certain uncertainties to rely on the relatively poor data quality of HCHO and the unsegregated multiple impacts of aerosols, such as N_2O_5 uptake, NO_2 uptake, HO_2 uptake and light extinction (Tan et al., 2022). We have made efforts to integrate all required surface pollutant concentrations into a unified model, while the absence of ground-level HCHO monitoring data compelled us to tap into an alternative methodology. The retrieval error of surface HCHO and the system error between its retrieval approach and the AiT model degrade the ability of ML to identify the O_3 sensitivity. Meanwhile, the notion of ozone regimes is only appreciated in photochemically active environments where the RO_x-HO_x cycle is active (Souri et al., 2023). The definition of NO_x-limited or VOC-limited is meaningless in nighttime chemistry, where NO-O_3-NO_2 partitioning is the primary driver. The surface daytime pollutant estimations with finer resolutions in space and time based on a unified modeling framework will offer an unprecedented view to characterize the near-surface O_3 formation regimes.

https://doi.org/10.5194/egusphere-2023-2640
Preprint. Discussion started: 18 December 2023

Competing Interests

The authors declare that they have no conflict of interest.

Acknowledgments

The work was financially supported by the National Natural Science Foundation of China (project No. 22236004) and Taishan Scholars (No. ts201712003).

Code and Data Availability

The Air Transformer deep learning framework is available on GitHub (https://github.com/myles-tcl/Air-Transformer), which provides the scripts for spatiotemporal data extraction, normalization, model training, and estimating of multi-pollutants. The sources of input data in the Air Transformer can be found in Table S1. The estimation of the Air Transformer can be downloaded from Zenodo: https://zenodo.org/records/10071408 (Tao, 2023).

Author Contributions

CT: Methodology, Software, Validation, Formal analysis, Investigation, Data Curation, Writing-Original Draft, Visualization. YP: Conceptualization, Writing-Review & Editing. QZ: Writing-Review & Editing, Project administration, Funding acquisition. YZ: Methodology, Writing-Review & Editing. BG: Software, Writing-Review & Editing. QW: Supervision, Writing-Review & Editing. WW: Supervision, Writing-Review & Editing.

https://doi.org/10.5194/egusphere-2023-2640
Preprint. Discussion started: 18 December 2023

References

Bertasius, G., Wang, H., and Torresani, L.: Is Space-Time Attention All You Need for Video Understanding?, http://arxiv.org/abs/2102.05095, 9 June 2021.

Breiman, L.: Random Forests, Machine Learning, 45, 5–32, https://doi.org/10.1023/A:1010933404324, 2001.

Chen, T. and Guestrin, C.: XGBoost: A Scalable Tree Boosting System, in: Proceedings of the 22nd ACM SIGKDD International Conference on Knowledge Discovery and Data Mining, KDD'16: The 22nd ACM SIGKDD International Conference on Knowledge Discovery and Data Mining, San Francisco California USA, 785–794, https://doi.org/10/gdp84q, 2016.

Action Plan on Air Pollution Prevention and Control (in Chinese): http://www.gov.cn/zwgk/2013-09/12/content_2486773.htm, last access: 1 February 2023.

Chu, W., Li, H., Ji, Y., Zhang, X., Xue, L., Gao, J., and An, C.: Research on ozone formation sensitivity based on observational methods: Development history, methodology, and application and prospects in China, Journal of Environmental Sciences, S1001074223000980, https://doi.org/10/gr4qzk, 2023.

Cooper, M. J., Martin, R. V., Hammer, M. S., Levelt, P. F., Veefkind, P., Lamsal, L. N., Krotkov, N. A., Brook, J. R., and McLinden, C. A.: Global fine-scale changes in ambient NO_2 during COVID-19 lockdowns, Nature, 601, 380–387, https://doi.org/10.1038/s41586-021-04229-0, 2022.

Copernicus Sentinel-5P (processed by ESA): TROPOMI Level 2 Ozone Total Column products. Version 02, European Space Agency, https://doi.org/10.5270/S5P-ft13p57, 2020.

Di, Q., Kloog, I., Koutrakis, P., Lyapustin, A., Wang, Y., and Schwartz, J.: Assessing $PM_{2.5}$ Exposures with High Spatiotemporal Resolution across the Continental United States, Environ. Sci. Technol., 50, 4712–4721, https://doi.org/10.1021/acs.est.5b06121, 2016.

Dias, D. and Tchepel, O.: Spatial and Temporal Dynamics in Air Pollution Exposure Assessment, IJERPH, 15, 558, https://doi.org/10.3390/ijerph15030558, 2018.

Didan, K.: MODIS/Terra Vegetation Indices 16-Day L3 Global 250m SIN Grid V061, NASA EOSDIS Land Processes Distributed Active Archive Center, https://doi.org/10.5067/MODIS/MOD13Q1.061, 2021.

https://doi.org/10.5194/egusphere-2023-2640
Preprint. Discussion started: 18 December 2023

667 van Donkelaar, A., Martin, R. V., Spurr, R. J. D., and Burnett, R. T.: High-Resolution
668 Satellite-Derived $PM_{2.5}$ from Optimal Estimation and Geographically Weighted
669 Regression over North America, Environ. Sci. Technol., 49, 10482–10491,
670 https://doi.org/10.1021/acs.est.5b02076, 2015.
671 Dosovitskiy, A., Beyer, L., Kolesnikov, A., Weissenborn, D., Zhai, X., Unterthiner, T.,
672 Dehghani, M., Minderer, M., Heigold, G., Gelly, S., Uszkoreit, J., and Houlsby,
673 N.: An Image is Worth 16x16 Words: Transformers for Image Recognition at
674 Scale, https://doi.org/10.48550/arXiv.2010.11929, 3 June 2021.
675 Dyson, J. E., Whalley, L. K., Slater, E. J., Woodward-Massey, R., Ye, C., Lee, J. D.,
676 Squires, F., Hopkins, J. R., Dunmore, R. E., Shaw, M., Hamilton, J. F., Lewis, A.
677 C., Worrall, S. D., Bacak, A., Mehra, A., Bannan, T. J., Coe, H., Percival, C. J.,
678 Ouyang, B., Hewitt, C. N., Jones, R. L., Crilley, L. R., Kramer, L. J., Acton, W. J.
679 F., Bloss, W. J., Saksakulkrai, S., Xu, J., Shi, Z., Harrison, R. M., Kotthaus, S.,
680 Grimmond, S., Sun, Y., Xu, W., Yue, S., Wei, L., Fu, P., Wang, X., Arnold, S. R.,
681 and Heard, D. E.: Impact of HO_2 aerosol uptake on radical levels and O_3
682 production during summertime in Beijing, Atmos. Chem. Phys., 23, 5679–5697,
683 https://doi.org/10/gshrst, 2023.
684 Geng, G., Xiao, Q., Liu, S., Liu, X., Cheng, J., Zheng, Y., Xue, T., Tong, D., Zheng,
685 B., Peng, Y., Huang, X., He, K., and Zhang, Q.: Tracking Air Pollution in China:
686 Near Real-Time $PM_{2.5}$ Retrievals from Multisource Data Fusion, Environ. Sci.
687 Technol., 55, 12106–12115, https://doi.org/10.1021/acs.est.1c01863, 2021.
688 Global Modeling and Assimilation Office (GMAO): MERRA-2 inst3_2d_gas_Nx: 2d,
689 3-Hourly, Instantaneous, Single-Level, Assimilation, Aerosol Optical Depth
690 Analysis V5.12.4, Greenbelt, MD, USA, Goddard Earth Sciences Data and
691 Information Services Center (GES DISC),
692 https://doi.org/10.5067/HNGA0EWW0R09, 2015.
693 Han, H., Zhang, L., Liu, Z., Yue, X., Shu, L., Wang, X., and Zhang, Y.: Narrowing
694 Differences in Urban and Nonurban Surface Ozone in the Northern Hemisphere
695 Over 1990–2020, Environ. Sci. Technol. Lett., 10, 410–417,
696 https://doi.org/10/gsd5gk, 2023.
697 Han, X. and Naeher, L. P.: A review of traffic-related air pollution exposure assessment
698 studies in the developing world, Environment International, 32, 106–120,
699 https://doi.org/10.1016/j.envint.2005.05.020, 2006.
700 Hersbach, H., Bell, B., Berrisford, G., Horányi, A., Muñoz Sabater, J., Nicolas, J.,

https://doi.org/10.5194/egusphere-2023-2640
Preprint. Discussion started: 18 December 2023

Peubey, C., Rozum, I., Schepers, D., Simmons, A., Soci, C., Dee, D., and Thépaut, J.-N.: ERA5 hourly data on single levels from 1959 to present, Copernicus Climate Change Service (C3S) Climate Data Store (CDS), https://doi.org/10.24381/cds.adbb2d47, 2023.

Huang, C., Hu, J., Xue, T., Xu, H., and Wang, M.: High-Resolution Spatiotemporal Modeling for Ambient $PM_{2.5}$ Exposure Assessment in China from 2013 to 2019, Environ. Sci. Technol., 55, 2152–2162, https://doi.org/10.1021/acs.est.0c05815, 2021.

Inness, A., Ades, M., Agustí-Panareda, A., Barré, J., Benedictow, A., Blechschmidt, A.-M., Dominguez, J. J., Engelen, R., Eskes, H., Flemming, J., Huijnen, V., Jones, L., Kipling, Z., Massart, S., Parrington, M., Peuch, V.-H., Razinger, M., Remy, S., Schulz, M., and Suttie, M.: The CAMS reanalysis of atmospheric composition, Atmos. Chem. Phys., 19, 3515–3556, https://doi.org/10/ghdkrm, 2019.

Ivatt, P. D., Evans, M. J., and Lewis, A. C.: Suppression of surface ozone by an aerosol-inhibited photochemical ozone regime, Nat. Geosci., 15, 536–540, https://doi.org/10.1038/s41561-022-00972-9, 2022.

Jerrett, M., Arain, A., Kanaroglou, P., Beckerman, B., Potoglou, D., Sahsuvaroglu, T., Morrison, J., and Giovis, C.: A review and evaluation of intraurban air pollution exposure models, Journal of Exposure Science & Environmental Epidemiology, 15, 185–204, https://doi.org/10.1038/sj.jea.7500388, 2005.

Jin, X., Fiore, A. M., Murray, L. T., Valin, L. C., Lamsal, L. N., Duncan, B., Folkert Boersma, K., De Smedt, I., Abad, G. G., Chance, K., and Tonnesen, G. S.: Evaluating a Space-Based Indicator of Surface Ozone-NO_x-VOC Sensitivity Over Midlatitude Source Regions and Application to Decadal Trends: Space-Based Indicator of O_3 Sensitivity, J. Geophys. Res. Atmos., 122, 10,439-10,461, https://doi.org/10.1002/2017JD026720, 2017.

Jin, X., Fiore, A., Boersma, K. F., Smedt, I. D., and Valin, L.: Inferring Changes in Summertime Surface Ozone-NO_x-VOC Chemistry over U.S. Urban Areas from Two Decades of Satellite and Ground-Based Observations, Environ. Sci. Technol., 54, 6518–6529, https://doi.org/10.1021/acs.est.9b07785, 2020.

Jin, X., Fiore, A. M., and Cohen, R. C.: Space-Based Observations of Ozone Precursors within California Wildfire Plumes and the Impacts on Ozone-NO_x-VOC Chemistry, Environ. Sci. Technol., 57, 14648–14660, https://doi.org/10.1021/acs.est.3c04411, 2023.

https://doi.org/10.5194/egusphere-2023-2640
Preprint. Discussion started: 18 December 2023

735 Jun, C., Ban, Y., and Li, S.: China: Open access to Earth land-cover map, Nature, 514,
736 434–434, https://doi.org/DOI:10.1038/514434c, 2014.
737 Jung, J., Choi, Y., Souri, A. H., Mousavinezhad, S., Sayeed, A., and Lee, K.: The
738 Impact of Springtime-Transported Air Pollutants on Local Air Quality With
739 Satellite-Constrained NO_x Emission Adjustments Over East Asia, Journal of
740 Geophysical Research: Atmospheres, 127, e2021JD035251,
741 https://doi.org/10.1029/2021JD035251, 2022.
742 Ke, G., Meng, Q., Finley, T., Wang, T., Chen, W., Ma, W., Ye, Q., and Liu, T.-Y.:
743 LightGBM: A Highly Efficient Gradient Boosting Decision Tree, in: Proceedings
744 of the 31st International Conference on Neural Information Processing Systems,
745 Red Hook, NY, USA, event-place: Long Beach, California, USA, 3149–3157,
746 2017.
747 Kohno, N., Zhou, J., Li, J., Takemura, M., Ono, N., Sadanaga, Y., Nakashima, Y., Sato,
748 K., Kato, S., Sakamoto, Y., and Kajii, Y.: Impacts of missing OH reactivity and
749 aerosol uptake of HO_2 radicals on tropospheric O_3 production during the AQUAS-
750 Kyoto summer campaign in 2018, Atmospheric Environment, 281, 119130,
751 https://doi.org/10/gshfc4, 2022.
752 Lamsal, L. N., Krotkov, N. A., Marchenko, S. V., Joiner, J., Oman, L., Vasilkov, A.,
753 Fisher, B., Qin, W., Yang, E.-S., Fasnacht, Z., Choi, S., Leonard, P., and Haffner,
754 D.: TROPOMI/S5P NO_2 Tropospheric, Stratospheric and Total Columns MINDS
755 1-Orbit L2 Swath 5.5 km x 3.5 km, Goddard Earth Sciences Data and Information
756 Services Center (GES DISC),
757 https://doi.org/10.5067/MEASURES/MINDS/DATA203, 2022.
758 Lee, H. J., Kuwayama, T., and FitzGibbon, M.: Trends of ambient O_3 levels associated
759 with O_3 precursor gases and meteorology in California: Synergies from ground
760 and satellite observations, Remote Sensing of Environment, 284, 113358,
761 https://doi.org/10.1016/j.rse.2022.113358, 2023.
762 Li, C., Zhu, Q., Jin, X., and Cohen, R. C.: Elucidating Contributions of Anthropogenic
763 Volatile Organic Compounds and Particulate Matter to Ozone Trends over China,
764 Environ. Sci. Technol., 56, 12906–12916, https://doi.org/10.1021/acs.est.2c03315,
765 2022a.
766 Li, D., Wang, S., Xue, R., Zhu, J., Zhang, S., Sun, Z., and Zhou, B.: OMI-observed
767 HCHO in Shanghai, China, during 2010–2019 and ozone sensitivity inferred by
768 an improved HCHO / NO_2 ratio, Atmos. Chem. Phys., 21, 15447–15460,

https://doi.org/10.5194/egusphere-2023-2640
Preprint. Discussion started: 18 December 2023

https://doi.org/10.5194/acp-21-15447-2021, 2021a.

Li, K., Jacob, D. J., Liao, H., Zhu, J., Shah, V., Shen, L., Bates, K. H., Zhang, Q., and Zhai, S.: A two-pollutant strategy for improving ozone and particulate air quality in China, Nat. Geosci., 12, 906–910, https://doi.org/10.1038/s41561-019-0464-x, 2019.

Li, K., Wang, Y., Peng, G., Song, G., Liu, Y., Li, H., and Qiao, Y.: UniFormer: Unified Transformer for Efficient Spatial-Temporal Representation Learning, International Conference on Learning Representations, 2021b.

Li, L. and Wu, J.: Spatiotemporal estimation of satellite-borne and ground-level NO_2 using full residual deep networks, Remote Sensing of Environment, 254, 112257, https://doi.org/10.1016/j.rse.2020.112257, 2021.

Li, M., Wang, T., Xie, M., Zhuang, B., Li, S., Han, Y., and Chen, P.: Impacts of aerosol-radiation feedback on local air quality during a severe haze episode in Nanjing megacity, eastern China, Tellus B: Chemical and Physical Meteorology, 69, 1339548, https://doi.org/10/gsfjz3, 2017.

Li, M., Yang, Q., Yuan, Q., and Zhu, L.: Estimation of high spatial resolution ground-level ozone concentrations based on Landsat 8 TIR bands with deep forest model, Chemosphere, 301, 134817, https://doi.org/10.1016/j.chemosphere.2022.134817, 2022b.

Lin, C., Huang, R.-J., Zhong, H., Duan, J., Wang, Z., Huang, W., and Xu, W.: Elucidating ozone and PM $_{2.5}$ pollution in the Fenwei Plain reveals the co-benefits of controlling precursor gas emissions in winter haze, Atmos. Chem. Phys., 23, 3595–3607, https://doi.org/10/gsfvs3, 2023.

Liu, M., Huang, Y., Ma, Z., Jin, Z., Liu, X., Wang, H., Liu, Y., Wang, J., Jantunen, M., Bi, J., and Kinney, P. L.: Spatial and temporal trends in the mortality burden of air pollution in China: 2004–2012, Environment International, 98, 75–81, https://doi.org/10.1016/j.envint.2016.10.003, 2017.

Liu, X., Shi, X., Lei, Y., and Xue, W.: Path of coordinated control of $PM_{2.5}$ and ozone in China, Chin. Sci. Bull., 67, 2089–2099, https://doi.org/10.1360/TB-2021-0832, 2022.

Lu, D., Mao, W., Zheng, L., Xiao, W., Zhang, L., and Wei, J.: Ambient $PM_{2.5}$ Estimates and Variations during COVID-19 Pandemic in the Yangtze River Delta Using Machine Learning and Big Data, Remote Sensing, 13, 1423, https://doi.org/10.3390/rs13081423, 2021.

https://doi.org/10.5194/egusphere-2023-2640
Preprint. Discussion started: 18 December 2023

803 Lu, X., Hong, J., Zhang, L., Cooper, O. R., Schultz, M. G., Xu, X., Wang, T., Gao, M.,
804 Zhao, Y., and Zhang, Y.: Severe Surface Ozone Pollution in China: A Global
805 Perspective, Environ. Sci. Technol. Lett., 5, 487–494,
806 https://doi.org/10.1021/acs.estlett.8b00366, 2018.
807 Lundberg, S. M. and Lee, S.-I.: A Unified Approach to Interpreting Model Predictions,
808 in: Proceedings of the 31st International Conference on Neural Information
809 Processing Systems, Red Hook, NY, USA, 2017.
810 Lyapustin, A. and Wang, Y.: MODIS/Terra+Aqua Land Aerosol Optical Depth Daily
811 L2G Global 1km SIN Grid V061, NASA EOSDIS Land Processes DAAC,
812 https://doi.org/10.5067/MODIS/MCD19A2.061, 2022.
813 Miller, D. F., Alkezweeny, A. J., Hales, J. M., and Lee, R. N.: Ozone Formation Related
814 to Power Plant Emissions, Science, 202, 1186–1188, https://doi.org/10/b5kgjr,
815 1978.
816 Mitchell, R., Frank, E., and Holmes, G.: GPUTreeShap: massively parallel exact
817 calculation of SHAP scores for tree ensembles, PeerJ Computer Science, 8,
818 https://doi.org/10.7717/peerj-cs.880, 2020.
819 Myers, S. L.: The Worst Dust Storm in a Decade Shrouds Beijing and Northern China,
820 The New York Times, 15th March, 2021.
821 Pusede, S. E., Steiner, A. L., and Cohen, R. C.: Temperature and Recent Trends in the
822 Chemistry of Continental Surface Ozone, Chem. Rev., 115, 3898–3918,
823 https://doi.org/10.1021/cr5006815, 2015.
824 Ren, J., Guo, F., and Xie, S.: Diagnosing ozone-NO_x-VOC sensitivity and revealing
825 causes of ozone increases in China based on 2013-2021 satellite retrievals, Atmos.
826 Chem. Phys., 22, 15035–15047, https://doi.org/10.5194/acp-22-15035-2022,
827 2022a.
828 Ren, X., Mi, Z., Cai, T., Nolte, C. G., and Georgopoulos, P. G.: Flexible Bayesian
829 Ensemble Machine Learning Framework for Predicting Local Ozone
830 Concentrations, Environ. Sci. Technol., 56, 3871–3883,
831 https://doi.org/10.1021/acs.est.1c04076, 2022b.
832 Requia, W. J., Di, Q., Silvern, R., Kelly, J. T., Koutrakis, P., Mickley, L. J., Sulprizio,
833 M. P., Amini, H., Shi, L., and Schwartz, J.: An Ensemble Learning Approach for
834 Estimating High Spatiotemporal Resolution of Ground-Level Ozone in the
835 Contiguous United States, Environ. Sci. Technol., 54, 11037–11047,
836 https://doi.org/10.1021/acs.est.0c01791, 2020.

https://doi.org/10.5194/egusphere-2023-2640
Preprint. Discussion started: 18 December 2023

837 Román, M. O., Wang, Z., Sun, Q., Kalb, V., Miller, S. D., Molthan, A., Schultz, L.,
838 Bell, J., Stokes, E. C., Pandey, B., Seto, K. C., Hall, D., Oda, T., Wolfe, R. E., Lin,
839 G., Golpayegani, N., Devadiga, S., Davidson, C., Sarkar, S., Praderas, C.,
840 Schmaltz, J., Boller, R., Stevens, J., Ramos González, O. M., Padilla, E., Alonso,
841 J., Detrés, Y., Armstrong, R., Miranda, I., Conte, Y., Marrero, N., MacManus, K.,
842 Esch, T., and Masuoka, E. J.: NASA's Black Marble nighttime lights product suite,
843 Remote Sensing of Environment, 210, 113–143, https://doi.org/10/ghqpjh, 2018.
844 Shapley, L. S.: A value for n-person games, in: The Shapley Value: Essays in Honor of
845 Lloyd S. Shapley, edited by: Roth, A. E., Cambridge University Press, Cambridge,
846 31–40, https://doi.org/10.1017/CBO9780511528446.003, 1988.
847 Shrikumar, A., Greenside, P., and Kundaje, A.: Learning Important Features Through
848 Propagating Activation Differences, http://arxiv.org/abs/1704.02685, 12 October
849 2019.
850 Sicard, P., Serra, R., and Rossello, P.: Spatiotemporal trends in ground-level ozone
851 concentrations and metrics in France over the time period 1999–2012,
852 Environmental Research, 149, 122–144,
853 https://doi.org/10.1016/j.envres.2016.05.014, 2016.
854 Sicard, P., De Marco, A., Agathokleous, E., Feng, Z., Xu, X., Paoletti, E., Rodriguez,
855 J. J. D., and Calatayud, V.: Amplified ozone pollution in cities during the COVID-
856 19 lockdown, Science of The Total Environment, 735, 139542,
857 https://doi.org/10/gg5w8h, 2020.
858 Sillman, S.: The use of NO_y, H_2O_2, and HNO_3 as indicators for ozone-NO_x-hydrocarbon
859 sensitivity in urban locations, J. Geophys. Res., 100, 14175,
860 https://doi.org/10.1029/94JD02953, 1995.
861 Song, H., Lu, K., Dong, H., Tan, Z., Chen, S., Zeng, L., and Zhang, Y.: Reduced
862 Aerosol Uptake of Hydroperoxyl Radical May Increase the Sensitivity of Ozone
863 Production to Volatile Organic Compounds, Environ. Sci. Technol. Lett., 9, 22–
864 29, https://doi.org/10/gnqqb9, 2022a.
865 Song, K., Liu, R., Wang, Y., Liu, T., Wei, L., Wu, Y., Zheng, J., Wang, B., and Liu, S.
866 C.: Observation-based analysis of ozone production sensitivity for two persistent
867 ozone episodes in Guangdong, China, Atmos. Chem. Phys., 22, 8403–8416,
868 https://doi.org/10/gr4qz2, 2022b.
869 Souri, A. H., Johnson, M. S., Wolfe, G. M., Crawford, J. H., Fried, A., Wisthaler, A.,
870 Brune, W. H., Blake, D. R., Weinheimer, A. J., Verhoelst, T., Compernolle, S.,

https://doi.org/10.5194/egusphere-2023-2640
Preprint. Discussion started: 18 December 2023

Pinardi, G., Vigouroux, C., Langerock, B., Choi, S., Lamsal, L., Zhu, L., Sun, S., Cohen, R. C., Min, K.-E., Cho, C., Philip, S., Liu, X., and Chance, K.: Characterization of errors in satellite-based HCHO/NO_2 tropospheric column ratios with respect to chemistry, column-to-PBL translation, spatial representation, and retrieval uncertainties, Atmospheric Chemistry and Physics, 23, 1963–1986, https://doi.org/10.5194/acp-23-1963-2023, 2023.

Su, W., Hu, Q., Chen, Y., Lin, J., Zhang, C., and Liu, C.: Inferring global surface HCHO concentrations from multisource hyperspectral satellites and their application to HCHO-related global cancer burden estimation, Environment International, 170, 107600, https://doi.org/10.1016/j.envint.2022.107600, 2022.

Sun, H., Shin, Y. M., Xia, M., Ke, S., Wan, M., Yuan, L., Guo, Y., and Archibald, A. T.: Spatial Resolved Surface Ozone with Urban and Rural Differentiation during 1990–2019: A Space–Time Bayesian Neural Network Downscaler, Environ. Sci. Technol., 56, 7337–7349, https://doi.org/10.1021/acs.est.1c04797, 2022.

Tan, Z., Lu, K., Ma, X., Chen, S., He, L., Huang, X., Li, X., Lin, X., Tang, M., Yu, D., Wahner, A., and Zhang, Y.: Multiple Impacts of Aerosols on O_3 Production Are Largely Compensated: A Case Study Shenzhen, China, Environ. Sci. Technol., 56, 17569–17580, https://doi.org/10/gsgp79, 2022.

Tang, L., Xue, X., Qu, J., Mi, Z., Bo, X., Chang, X., Wang, S., Li, S., Cui, W., and Dong, G.: Air pollution emissions from Chinese power plants based on the continuous emission monitoring systems network, Sci Data, 7, 325, https://doi.org/10/ghfqqf, 2020.

Tao, C.: Surface Ozone, NO_2, and $PM_{2.5}$ Concentrations Estimated by the Deep Learning model (Air Transformer) based on Satellite data, https://doi.org/10.5281/zenodo.10071408, 2023.

Thongthammachart, T., Araki, S., Shimadera, H., Matsuo, T., and Kondo, A.: Incorporating Light Gradient Boosting Machine to land use regression model for estimating NO_2 and $PM_{2.5}$ levels in Kansai region, Japan, Environmental Modelling & Software, 155, 105447, https://doi.org/10.1016/j.envsoft.2022.105447, 2022.

Wei, J., Li, Z., Cribb, M., Huang, W., Xue, W., Sun, L., Guo, J., Peng, Y., Li, J., Lyapustin, A., Liu, L., Wu, H., and Song, Y.: Improved 1 km resolution $PM_{2.5}$ estimates across China using enhanced space–time extremely randomized trees, Atmos. Chem. Phys., 20, 3273–3289, https://doi.org/10.5194/acp-20-3273-2020,

https://doi.org/10.5194/egusphere-2023-2640
Preprint. Discussion started: 18 December 2023

2020.

Wei, J., Li, Z., Li, K., Dickerson, R. R., Pinker, R. T., Wang, J., Liu, X., Sun, L., Xue, W., and Cribb, M.: Full-coverage mapping and spatiotemporal variations of ground-level ozone (O_3) pollution from 2013 to 2020 across China, Remote Sensing of Environment, 270, 112775, https://doi.org/10.1016/j.rse.2021.112775, 2022a.

Wei, J., Liu, S., Li, Z., Liu, C., Qin, K., Liu, X., Pinker, R. T., Dickerson, R. R., Lin, J., Boersma, K. F., Sun, L., Li, R., Xue, W., Cui, Y., Zhang, C., and Wang, J.: Ground-Level NO_2 Surveillance from Space Across China for High Resolution Using Interpretable Spatiotemporally Weighted Artificial Intelligence, Environ. Sci. Technol., acs.est.2c03834, https://doi.org/10.1021/acs.est.2c03834, 2022b.

Wei, W., Wang, X., Wang, X., Li, R., Zhou, C., and Cheng, S.: Attenuated sensitivity of ozone to precursors in Beijing–Tianjin–Hebei region with the continuous NOx reduction within 2014–2018, Science of The Total Environment, 813, 152589, https://doi.org/10/gq7ngn, 2022c.

WorldPop: Global High Resolution Population Denominators Project - Funded by The Bill and Melinda Gates Foundation (OPP1134076)., https://dx.doi.org/10.5258/SOTON/WP00675, 2018.

Xiao, Q., Chang, H. H., Geng, G., and Liu, Y.: An Ensemble Machine-Learning Model To Predict Historical $PM_{2.5}$ Concentrations in China from Satellite Data, Environ. Sci. Technol., 52, 13260–13269, https://doi.org/10.1021/acs.est.8b02917, 2018.

Yue, X., Unger, N., Harper, K., Xia, X., Liao, H., Zhu, T., Xiao, J., Feng, Z., and Li, J.: Ozone and haze pollution weakens net primary productivity in China, Atmospheric Chemistry and Physics, 17, 6073–6089, https://doi.org/10.5194/acp-17-6073-2017, 2017.

Zhang, J., Wang, J., Sun, Y., Li, J., Ninneman, M., Ye, J., Li, K., Crandall, B., Mao, J., Xu, W., Schwab, M. J., Li, W., Ge, X., Chen, M., Ying, Q., Zhang, Q., and Schwab, J. J.: Insights from ozone and particulate matter pollution control in New York City applied to Beijing, npj Clim Atmos Sci, 5, 85, https://doi.org/10/gr8rtz, 2022.

Zhang, R., Lei, W., Tie, X., and Hess, P.: Industrial emissions cause extreme urban ozone diurnal variability, Proc. Natl. Acad. Sci. U.S.A., 101, 6346–6350, https://doi.org/10.1073/pnas.0401484101, 2004.

Zhao, M., Cheng, C., Zhou, Y., Li, X., Shen, S., and Song, C.: A global dataset of annual urban extents (1992–2020) from harmonized nighttime lights, Earth

https://doi.org/10.5194/egusphere-2023-2640
Preprint. Discussion started: 18 December 2023

939 System Science Data, 14, 517–534, https://doi.org/10.5194/essd-14-517-2022,
940 2022.
941 Zheng, B., Tong, D., Li, M., Liu, F., Hong, C., Geng, G., Li, H., Li, X., Peng, L., Qi, J.,
942 Yan, L., Zhang, Y., Zhao, H., Zheng, Y., He, K., and Zhang, Q.: Trends in China's
943 anthropogenic emissions since 2010 as the consequence of clean air actions,
944 Atmos. Chem. Phys., 18, 14095–14111, https://doi.org/10.5194/acp-18-14095-
945 2018, 2018.
946